Supplementary information for "Robust quantum-network memory based on spin qubits in isotopically engineered diamond"

C. E. Bradley[1,2], S. W. de Bone[1,3], P. F. W. Möller[1], S. Baier[1,2], M. J. Degen[1,2], S. J. H. Loenen[1,2], H. P. Bartling[1,2], M. Markham[4], D. J. Twitchen[4], R. Hanson[1,2], D. Elkouss[1], and T. H. Taminiau[1,2,†]
[1] *QuTech, Delft University of Technology, 2628 CJ Delft, The Netherlands*
[2] *Kavli Institute of Nanoscience, Delft University of Technology, 2628 CJ Delft, The Netherlands*
[3] *QuSoft, Centrum Wiskunde & Informatica, 1098 XG, Amsterdam, The Netherlands and*
[4] *Element Six Innovation, Fermi Avenue, Harwell Oxford, Didcot, Oxfordshire, OX110QR, United Kingdom*
(Dated: September 22, 2022)

Supplementary Note 1: Active link efficiency

In the main text, we introduce the 'active' link efficiency, $\eta^*_{\text{link}} = r_{\text{ent}}/r_{\text{dec}}$, given by the ratio of the inter-node entanglement generation rate r_{ent} and the decoherence rate r_{dec} of the data qubits during network operation. This is a slight modification to the passive version of the link efficiency introduced in prior work, η_{link}, which was evaluated considering r_{dec} to be the decoherence rate of a two-qubit entangled state during *idling* of the communication link, rather than the single-qubit rate during remote entanglement operation [1]. That metric relates specifically to deterministic entanglement delivery on a clock cycle [1] and bounds η^*_{link}. A large η_{link} is a necessary, but not sufficient condition for large quantum networks. While previous experiments reported η_{link} in the range of 5-8 [1, 2], the η^*_{link} in those works was much smaller than 1.

Supplementary Note 2: Nuclear-spin control

Dynamical decoupling (DD) spectroscopy is used to characterise the nuclear spin environment of the NV centre [3]. The signal presented in the main text (Fig. 1(c)) is modelled by the interaction of the NV with two individual ^{13}C spins, taking into account the decoherence of the electron spin during the decoupling sequence [3].

The resonance at 44.832 μs is associated with the single spin characterised as a data qubit in this work, for which we extract hyperfine interaction parameters of $A_\parallel = 2\pi\cdot$ 80(1) Hz and $A_\perp = 2\pi\cdot$ 271(4) Hz via Ramsey spectroscopy and DD nutation experiments respectively [4]. The resonance at 44.794 μs is, in reality, a sum over a number of spins associated with the ^{13}C bath. However, the signal is reasonably approximated by a single nuclear spin with $A_\parallel = 2\pi\cdot$ 0 Hz and $A_\perp = 2\pi\cdot$ 150 Hz.

We realise universal control over the electron-^{13}C system: an electron-nuclear two-qubit gate is implemented following the methods described in Taminiau *et al.* [5] (CRot duration ∼ 25 ms), while selective radio-frequency driving and free precession enable arbitrary ^{13}C single-qubit gates [6]. Following the methods of Cramer *et al.*, we estimate the two-qubit gate fidelity to be ∼ 84% [7]. This is thought to be limited by the electron spin coherence, which is restricted by the P1 spin bath rather than the ^{13}C bath. Reduction of these impurities through improved diamond growth should enable high fidelity control over a larger number of nuclear spins, as demon-

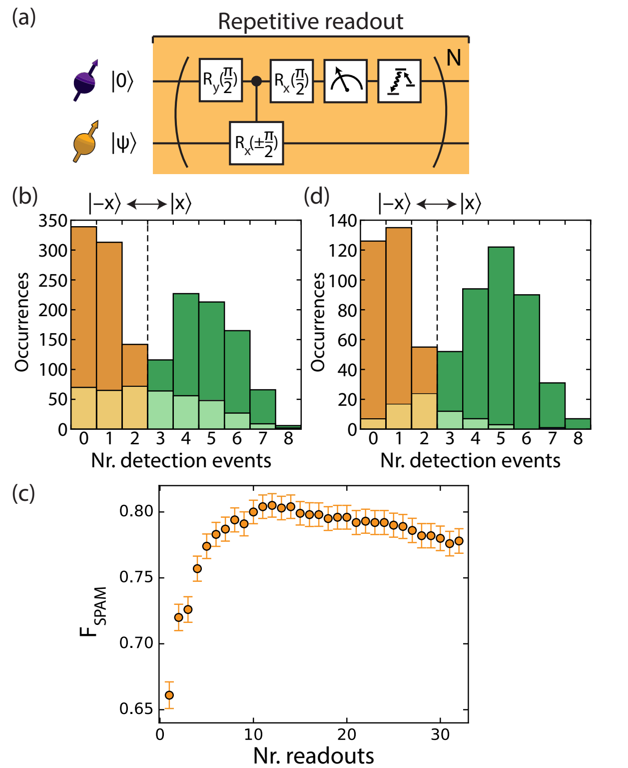

Supplementary Figure 1. **Nuclear spin repetitive readout:** (a) Repetitive readout protocol: in each repetition, the nuclear X-basis spin-projection is mapped to the electron spin Z-basis, which is optically read out and then reset. (b) Example histograms obtained when preparing the $|x\rangle$ and $|-x\rangle$ states with a single projective measurement, followed by 8 X-basis readouts. Dashed line denotes the optimal state discrimination threshold. Dark (light) colours correspond to populations which are assigned to the targeted (erroneous) state. (c) Optimised state preparation and measurement fidelity as a function of the number of repetitive readouts. (d) Same as (b), but now using the outcomes of 8 prior readouts ($\geq$5 read-outs with $\geq$1 photon for $|x\rangle$ initialisation, no photons in any of the 8 readouts for $|-x\rangle$ initialisation) as an additional initialisation step.

strated in natural abundance ^{13}C samples [6].

As the fidelity of the nuclear spin readout is limited by the electron spin coherence, it is possible to improve this readout fidelity by repeated measurements, as has previously been achieved for single ^{13}C nuclear spins under ambient conditions [8–10]. We implement the repetitive readout protocol shown in Supplementary Fig. 1(a). As the electron-nuclear coupling is weak — $A_{\parallel} \ll 1/\tau_{\mathrm{RO}}$, for τ_{RO} the combined readout and repumping time — electron spin flips during the optical readout induce minimal ^{13}C dephasing. We can thus repeat the mapping and readout procedure a number of times, from which we acquire histograms as exemplified in Supplementary Fig. 1(b).

The histograms after preparation of $|\mathrm{x}\rangle$ and $|{-\mathrm{x}}\rangle$ respectively show two distinct populations. The state preparation and measurement process is quantified by $F_{\mathrm{SPAM}} = \frac{1}{2}(F_{\mathrm{x}|\mathrm{x}} + F_{-\mathrm{x}|-\mathrm{x}})$, where $F_{i|j}$ is the probability to assign the spin state $|i\rangle$ after attempting initialisation in $|j\rangle$. In Supplementary Fig. 1(c), we plot F_{SPAM} as a function of the number of repeated readouts, in each case using the optimal threshold to discriminate the two states. At an optimum number of 12 readouts, F_{SPAM} reaches 80.4(9)%. In all nuclear spin data shown in the main text and in the remainder of this supplement, we utilise N = 8 readout repetitions (F_{SPAM} = 79.4(9)%) as a trade-off between optimal fidelity and measurement run-time. The associated histogram is shown in Supplementary Fig. 1(b).

F_{SPAM} is predominantly limited by two mechanisms. First, the measurement sequence still induces some decoherence of the nuclear spin — as can be seen by the decrease in fidelity for >12 read-outs — reducing the extractable information. This effect would likely be mitigated by improvement of the two-qubit gate. Second, we prepare the $|\mathrm{x}\rangle$ and $|{-\mathrm{x}}\rangle$ states using a single projective measurement [7]. Repetitive measurements can also be used to initialise the spin: in Supplementary Fig. 1(d) we additionally show the outcome of 8 repetitive readouts, conditioned on the outcome of 8 prior readouts. We find an achievable F_{SPAM} = 91(1)%, but do not employ it in this work due to the additional time overhead of >0.5 s per experimental shot.

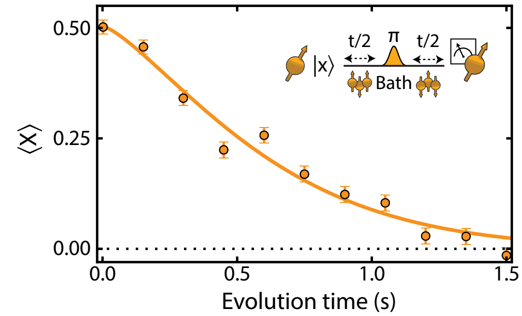

Supplementary Figure 2. **^{13}C spin-bath echo:** Measured nuclear spin dephasing when applying a spin-echo at the ^{13}C Larmor frequency. The electron is initialised in the $|0\rangle$ state, such that the echo pulse simultaneously inverts the addressed ^{13}C along with the surrounding nuclear spin environment. The data are fit with an exponential decay, $f(t) = A\exp[-(t/T_2)^n]$, for which we find $T^*_{2,^{13}\mathrm{C-bath}}$ = 0.66(3) s and $n = 1.3(1)$.

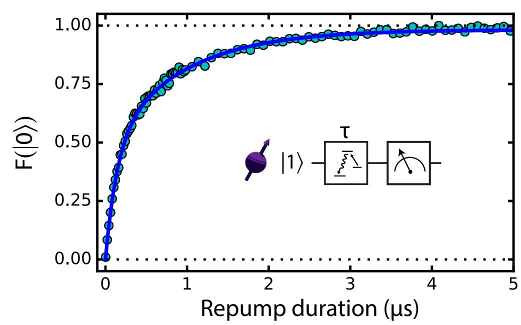

Supplementary Figure 3. **Electron spin reset:** After initialisation in $|1\rangle$, the population in $|0\rangle$ is plotted as a function of the repumping duration (30 nW, E'). A delay of 10 μs between turning off the spin-pumping laser and turning on the readout laser ensures that minimal population resides in the metastable singlet states [11]. The data are well described by a two-timescale phenomenological model: $f(t) = A(1 - \exp[-t/\tau_1]) + B(1 - \exp[-t/\tau_2])$, for which we find A=0.480(15), B=0.503(14), τ_1=142(5) ns, τ_2=905(31) ns.

Supplementary Note 3: ^{13}C spin-bath echo

In the main text, we report the nuclear spin dephasing timescale associated with nuclear spin bath dynamics to be $T^*_{2,^{13}\mathrm{C-bath}} = 0.66(3)$ s. To identify this timescale, we prepare the electron in the $|0\rangle$ state and perform a spin-echo at the ^{13}C Larmor frequency (Ω_{Rabi} = 120 Hz). Such a pulse inverts the local nuclear spin environment, decoupling it from other quasi-static noise sources but leaving the ^{13}C-^{13}C interactions unperturbed.

In Supplementary Fig. 2 we present the measured data and experimental sequence.

Supplementary Note 4: Electron spin initialisation

Electron spin initialisation constitutes a large fraction of the remote entanglement primitive duration [12]. Therefore, faster initialisation rates are desirable. This can be achieved by using higher laser powers, such that the NV centre is more frequently excited. However, higher laser powers also increase the ionisation rate [13, 14]. Furthermore, as initialisation occurs primarily via the NV$^-$ intersystem crossing [11], the $\sim$ 370 ns lifetime of the singlet state, alongside the finite branching ratio from this state to the targeted $m_s = 0$ state, limit the extent to which higher laser powers increase the reset speed.

As a trade-off between these factors, we use 30 nW of E' excitation for the repumping process. This leads to initialisation fidelities ≥98% in a duration of 5 μs. In Supplementary Fig. 3 we plot the measured reset dynamics for this power.

Supplementary Note 5: Weak electron-spin pulses

When implementing large numbers of repetitions of the remote entanglement protocol using strong microwave pulses, the mean number of detected photons during single-shot read-out was observed to decrease. This is attributed to heating of the sample. Note that heating is problematic in the context of optical entanglement generation, because a reduction of the photon emission decreases the success probability, and the photon indistinguishability also decreases with temperature [15].

The applied heat-load can be reduced by decreasing the MW Rabi frequency, but this is complicated by the presence of the nitrogen nuclear-spin. The electron-nitrogen hyperfine coupling, $A_\parallel S_z I_z$ ($A_\parallel = 2\pi \cdot 2.18$ MHz) causes a three-fold splitting of the transition frequency. For this reason, we usually employ strong, spectrally-broad Hermite pulses (Rabi frequency ~ 27 MHz) for high-fidelity ($\gg 99\%$) manipulation of the electron spin, independent of the nitrogen spin state.

While prior initialisation of the nitrogen spin in a chosen state can relax this requirement [16], the large excited-state hyperfine coupling causes rapid depolarisation of the nuclear spin under repeated optical reset of the electron-spin, ruling out this method in the presented experiments [17].

An alternative approach is to apply three separate drive tones, each addressing one of the nitrogen hyperfine levels. High-fidelity inversion is realised if the Rabi frequency of each tone, Ω, is large relative to the transition linewidth, which is described by a Gaussian distribution with $\sigma_f = 1/(\sqrt{2}\pi T_2^*) = 4.5$ kHz. Conversely, Ω should be small relative to the detuning between the transitions $A_\parallel$, such that AC-Stark frequency shifts remain small. We apply square pulse envelopes with $\Omega = 92$ kHz for each tone. The integrated power over the multi-tone pulse is ~ 80 (~ 40) times reduced for the π ($\pi/2$) pulse when compared to the strong Hermite pulses (Rabi frequency: π-pulse ~ 27 MHz, $\pi/2$-pulse ~ 16 MHz), enabling the repeated application of hundreds of thousands of MW pulses without observation of heating effects.

We numerically evaluate the electron spin dynamics using the QuTip python package [18]. Making the secular and rotating wave approximations, and transforming to the interaction picture $\omega_1 \hat{S}_z$, with $\omega_1 = D + \gamma_e B_z$, the Hamiltonian describing the evolution of the driven electron-nitrogen system is:

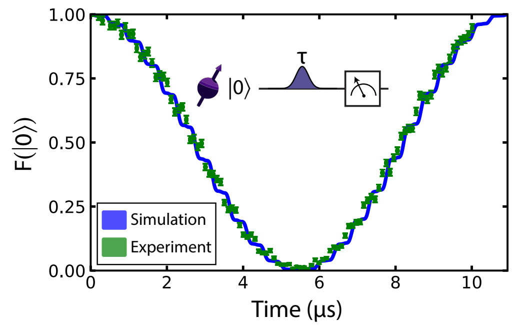

Supplementary Figure 4. **Weak microwave pulses:** Electron spin dynamics under application of the three-tone microwave pulse. The solid line (circles) show the simulated (measured) dynamics after initialisation of the electron spin in $|0\rangle$. A π-pulse is realised after 5.5 μs.

$$\begin{aligned} H' = {} & 2D\,|2\rangle\langle 2| + Q\hat{I}_z^2 + \gamma_N B_z \hat{I}_z + A_\parallel \hat{S}_z \hat{I}_z \\ & + \frac{1}{\sqrt{2}}\Omega(\cos(\phi_1)\hat{S}_x - \sin(\phi_1)\hat{S}_y) \\ & + \frac{1}{\sqrt{2}}\Omega(\cos(A_\parallel t + \phi_2)\hat{S}_x - \sin(A_\parallel t + \phi_2)\hat{S}_y) \\ & + \frac{1}{\sqrt{2}}\Omega(\cos(-A_\parallel t + \phi_3)\hat{S}_x - \sin(-A_\parallel t + \phi_3)\hat{S}_y). \end{aligned} \tag{1}$$

Here, $\hat{S}_i$ and $\hat{I}_i$ are the electron and nuclear spin-1 operators. D is the zero-field splitting, Q is the quadrupole splitting, γ_e and γ_N are the electron and nitrogen gyromagnetic ratios, and B_z is the external magnetic field component parallel to the NV axis. ϕ_i are the phases of the individual drive fields, while $|2\rangle\langle 2|$ is the projector on the state $|2\rangle$ of the electron spin: this term is a detuning of the non-driven $m_s = +1$ electron spin transition. We have additionally assumed that the three drive tones are x-polarised.

In Supplementary Fig. 4 we show the simulated and measured electron spin dynamics. A high-fidelity π-pulse is realised after ~ 5.5 μs of driving. The observed modulations arise due to slight relative AC-Stark shifts. Each drive tone induces a frequency shift approximately given by $\delta_{\mathrm{AC-Stark}} \sim \Omega^2/2\Delta$, where Δ is the difference between the drive frequency and each detuned transition frequency. For the $m_I = 0$ transition, the shifts from the off-resonant tones are cancelled to first order. However, for the $m_I = \pm 1$ transitions, there is a frequency shift of $\sim \pm 2$ kHz.

We note that the parameters used here are not suitable for natural abundance samples, ($T_2^* \sim 5\,\mu$s, $1/(\sqrt{2}\pi T_2^*) \sim 45$ kHz), where the broader intrinsic linewidth leads to significant infidelity (simulated to be $\sim 33\%$ by Monte Carlo sampling, compared with $\sim 0.6\%$ for the present scenario). However, heating can alternatively be addressed by improved device engineering in future work, for example by fabricating the stripline using superconducting materials. This would enable the use of strong microwave pulses throughout the experiments and remove the time overhead required for weak pulses.

Supplementary Note 6: Quantum network memory performance using strong pulses

As discussed in the above section, the use of strong microwave pulses during the remote entanglement primitive led to the observation of heating effects. For this reason, we implemented the weak pulse scheme to ensure that optical processes were unaffected and thus would be compatible with remote entanglement generation. Nevertheless, we here study the data qubit decoherence when using strong pulses, which enables a shorter duration per entangling attempt.

The entangling primitive used here is identical to that used in the main text ($t_\mathrm{r} = 5$ μs, $t' = 200$ ns, $t_1 = 1$ μs), but with the weak MW $\pi/2$ pulse ($t_\mathrm{MW} = 2.8$ μs) now replaced by a Hermite $\pi/2$ pulse ($t_\mathrm{MW} = 100$ ns). The total duration is thus reduced from 9 μs to 6.3 μs. We measure the decay of the nuclear coherence, $(\langle X\rangle^2 + \langle Y\rangle^2)^{1/2}$, as a function of the number of entangling primitives after initialisation in $|\mathrm{x}\rangle$. We again interleave one round of nuclear spin XY8 decoupling pulses. In Supplementary Fig. 5 we plot the results, including different post-selection thresholds for the post-measurement CR checks as in the main text. Importantly, the rejected fraction of events is similar to that observed when using the weak pulse scheme, suggesting that optical dynamics are relatively unchanged.

When compared with the data presented in the main text, we observe an increase in data qubit robustness. With the most stringent filtering, we find a decay time of $419(96)\cdot 10^3$ attempts (2.6(6) s). This compares favourably with the weak pulse case, where the equatorial states $\{|\mathrm{x}\rangle, |\mathrm{y}\rangle, |{-\mathrm{x}}\rangle, |{-\mathrm{y}}\rangle\}$ have a mean decay time of $190(8)\cdot 10^3$ attempts (1.8(1) s).

Supplementary Note 7: Simulated nuclear spin dephasing due to the remote-entanglement protocol

In this section we numerically analyse the nuclear-spin dephasing induced by repeated remote entanglement attempts. Our analysis is based upon Monte Carlo simulations, adapted from the work of Kalb *et al.* [11]. Here, we will neglect the intrinsic dephasing timescales (T_2^* and T_2) of the nuclear spin, rather focusing on the limits imposed by the remote entanglement sequence alone. Further, we neglect the role played by ionisation. We will consider two sequences, the first following that implemented experimentally, and the second in which an additional electron spin-echo is incorporated within each attempt, see Supplementary Figs. 6(a,b).

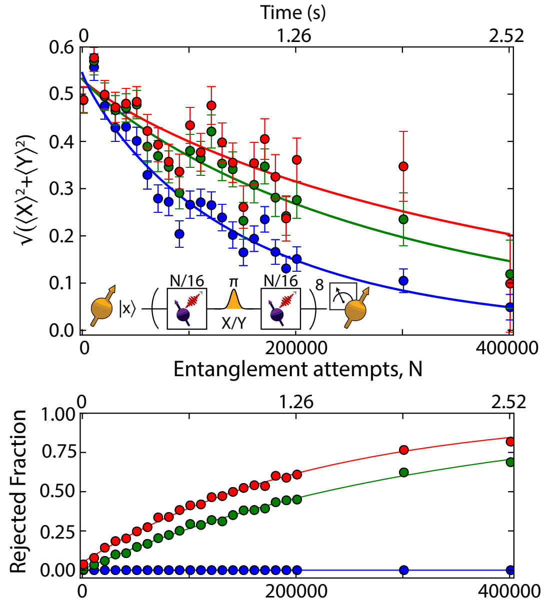

Supplementary Figure 5. **Data qubit robustness using strong electron pulses:** Nuclear spin coherence as a function of the number of applied remote entangling primitives. Blue, green, red lines correspond to post-selection using a CR-check performed after the experiment, with thresholds of 0, 1, 5 respectively. The lower panel shows the corresponding fraction of rejected data.

To build up a statistical distribution for the phase acquired by the nuclear spin after repeated application of the sequence, we generate a number of samples, K, each of N trials.

In each trial, a random number $0 \leq \mathrm{R_{init}} \leq 1$ is used to instantiate the NV electron in a given spin projection, $|s\rangle \in \{-1, 0, +1\}$, each with probability $p_{|s\rangle}$. The $p_{|s\rangle}$ are parameterised by a chosen initialisation error, p_init, such that $p_{|0\rangle} = (1 - p_\mathrm{init})$ and $p_{|-1\rangle} = p_{|+1\rangle} = p_\mathrm{init}/2$.

The nuclear spin is now evolved for a time, $t_\mathrm{a} = (t_\mathrm{p} - \langle t_c\rangle + t_\mathrm{s})$, where t_p is the total optical pumping duration, $\langle t_c\rangle$ is the mean time to initialise ('reset') the spin, and t_s is the spacing between the end of the repump laser pulse and the centre of the 'α' microwave pulse (used to prepare the electron superposition for spin-photon entanglement). The stochastic nature of t_c is accounted for below. A phase, ϕ_a is acquired according to the initial state, at the difference frequency $\delta\omega = A_\parallel s$.

Next, the 'α' microwave pulse is applied, the effect of which is treated as instantaneous. While throughout this work we set $\alpha = \pi/2$, for which the sequence induces maximal dephasing noise on the data qubit, α is generally a free parameter which determines a rate-fidelity trade-off for remote spin-spin entanglement in the single-click entangling protocol [1, 12]. Another random number, $0 \leq \mathrm{R_{MW}} \leq 1$, is used to determine whether the electron spin is flipped between $|0\rangle \leftrightarrow |-1\rangle$ ($|+1\rangle$ is assumed to be unperturbed). The inversion is applied if $\mathrm{R_{MW}} < p_\mathrm{MW}$, the inversion probability of the chosen microwave pulse.

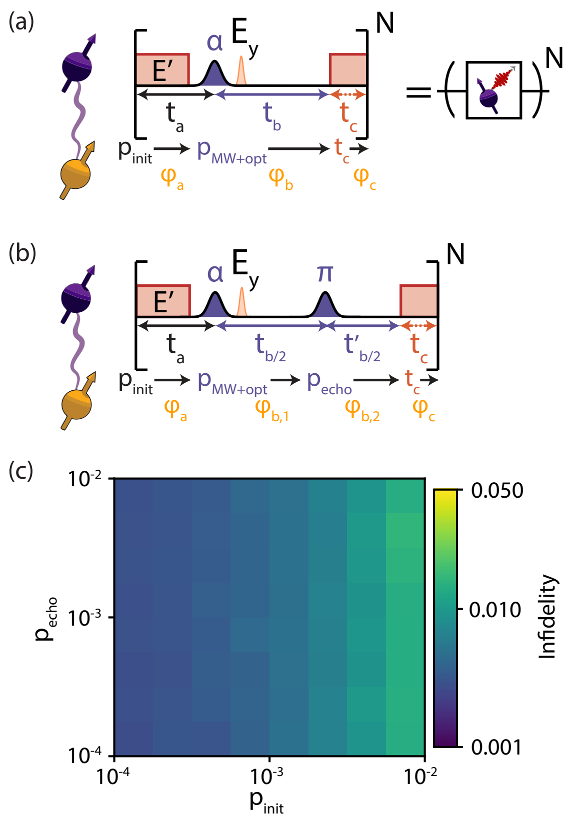

Supplementary Figure 6. **Numerical analysis of nuclear spin dephasing:** (a) Sketch of the primitive remote entanglement unit used in experiment as formulated for Monte Carlo simulation. The nuclear spin (yellow) acquires spurious phases according to the dynamics of the electron spin (purple) and the $\hat{S}_z\hat{I}_z$ coupling $A_\parallel$. This phase is broken down into contributions from three imperfect operations, determined by initialisation infidelity (ϕ_a, parameterised by $p_{\rm init}$), microwave inversion (ϕ_b, parameterised by $p_{\rm MW}$ and $p_{\rm opt}$) and stochastic reset time (ϕ_c, parameterised by t_c). (b) Sketch of the primitive remote entanglement unit when incorporating an additional electron spin-echo pulse (with failure possibility parameterised by $p_{\rm echo}$). (c) Results of Monte Carlo simulations for the scenario given in (b), after application of 10^6 entangling primitives. $\alpha = \pi/2$, $p_{\rm MW} = 0.5$, $p_{\rm opt} = 0.01$, $t_a = 5.1\ \mu$s, $t_b = 1.3\ \mu$s and $\langle t_c \rangle = 200$ ns. Results are averaged over 1000 samples.

Immediately after the microwave pulse, we apply the effect of the optical π-pulse used to create spin-photon entanglement. A third random number, $0 \leq \mathrm{R}_{\rm opt} \leq 1$, is used to determine whether the electron spin is flipped from $|0\rangle \rightarrow \{|-1\rangle, |+1\rangle\}$, each with equal probability. Again, the inversion is applied if $\mathrm{R}_{\rm opt} < p_{\rm opt}$, which we set to be 0.01, according to the estimated spin-flip probability of the $\mathrm{E}_{\rm x,y}$ transitions [11]. Note that the probability of this spin-flip is much smaller than that induced by the microwave pulse, justifying the omission of the optical pulses in the presented experiments.

In the case that we do not incorporate the electron spin-echo (Supplementary Fig. 6(a)), the nuclear spin now simply acquires phase for a time t_b (ϕ_b), defined as the time between the centre of the microwave pulse and the onset of optical pumping. This time period allows for the decision logic for success or failure of the remote entanglement protocol (detection or loss of the optical photon). For short range (metre-scale) experiments, this timescale is typically $\sim 1\,\mu s$, limited by the current electronics used. The dephasing associated with t_b is dominant in this sequence: for $\alpha = \pi/2$, there is an extended period of time during which the electron has an approximately 50% chance to be in either the $|0\rangle$ or $|-1\rangle$ state.

Finally, we account for the stochastic optical reset. In the case that the electron spin is in $|-1\rangle$ or $|+1\rangle$ at the onset of spin-pumping, a finite duration is required to prepare $|0\rangle$ for the start of the next repetition. A reset time, t_c, is sampled from the phenomenological two-timescale function fitted in Supplementary Fig. 3, which determines the final evolution time before the end of the trial, during which time a phase ϕ_c is acquired.

Summing these phases, we find the total phase acquired by the nuclear spin for the i-th trial of the k-th sample: $\phi_{i,k}$. Repeating this process for N trials, we calculate the cumulative phases $\Phi_{n,k} = \sum_{i=1}^{n} \phi_{i,k}$ for $n = \{1, ..., N\}$.

For each sample, we can then calculate the state fidelity after each n trials:

$$F_{n,k} = \frac{1}{2} + \frac{1}{2}\cos(\Phi_{n,k} - \overline{\Phi_n}) \tag{2}$$

where $\overline{\Phi_n}$ is the mean phase after n trials, averaged over all samples. Finally, we find the characteristic n for which $\cos(\Phi_{n,k} - \overline{\Phi_n})$ falls below $1/e$.

As the dephasing associated with t_b is dominant, we also consider the case in which it is possible to incorporate an additional spin-echo into the sequence (for example, because heating is mitigated by device engineering), see Supplementary Fig. 6(b). In this case, the nuclear spin acquires phase for a time $t_b/2$ ($\phi_{b,1}$), before the echo is applied, and then for a further time $(t_b'/2 + \langle t_c \rangle) = t_b/2$ ($\phi_{b,2}$). In case of successful application of the echo, $\phi_{b,1} + \phi_{b,2} = 0$. We account for a finite failure probability of the echo pulse using another random number, $0 \leq \mathrm{R}_{\rm echo} \leq 1$. If $\mathrm{R}_{\rm echo} > p_{\rm echo}$, the electron spin is flipped between $|0\rangle \leftrightarrow |-1\rangle$.

We consider two regimes. First, for the sequence excluding the spin-echo, we choose parameters that are as least as pessimistic as used in the experiments in the main text. We have $t_a = 6.1\ \mu$s, $t_b = 2.4\ \mu$s, $\langle t_c \rangle = 535$ ns (following the two-timescale function fitted in Fig. 3), $p_{\rm init} = 0.03$, $p_{\rm MW} = 0.5$, $p_{\rm opt} = 0.01$. We find that after application of 10^6 entangling primitives, the expected fidelity with an initial superposition state is 0.776(4), averaged over $K = 4000$ samples. These calculations indicate that dephasing due to the entangling sequence is not limiting in the experiments.

We now turn to the case in which the echo is incorporated. We assume that strong MW pulses can be employed, enabling $t_a = 5.1$ μs, $t_b = 1.3$ μs. Further, we assume that faster spin reset can be achieved, as has been previously demonstrated with higher powers [11, 19]: setting $\langle t_c \rangle = 200$ ns (following a single exponential timescale). We set $p_{\mathrm{MW}} = 0.5$, $p_{\mathrm{opt}} = 0.01$. We now perform a 2D sweep of the fidelity after 10^6 trials as a function of p_{init} and p_{echo}. The results are plotted in Supplementary Fig. 6(c). Even with 1% errors in the initialisation and echo operations, a fidelity of 0.975(1) is achieved. Note that the errors associated with initialisation are dominant over those associated with echo failure for these timings. This is because, first, $t_a > t_b$, and, second, this process can erroneously prepare the electron $|s\rangle = +1$ state. In particular, during the time t_b, the memory ideally evolves at the average frequency associated with the electron $|s\rangle = \{-1, 0\}$ states. Instances in which the $|s\rangle = +1$ state occurs lead to t_b evolution at a frequency difference 3 times larger than cases in which the echo fails (which result in t_b evolution with either $|s\rangle = 0$ or -1).

Supplementary Note 8: Controlled charge-state switching of the NV centre

Throughout the experiments shown in this work, we make use of two-laser probe measurements ('CR checks') to detect the NV$^-$ charge state [15]. During these checks, weak resonant light is applied on the NV$^-$ E' (8 nW) and $\mathrm{E_y}$ (1.5 nW) transitions for 150 μs, during which we record all photon counts. By setting a threshold on the number of detected photons, it is possible to herald that the NV is in the negative charge-state, and that the spin-pumping and readout lasers are resonant. In the case of low counts a strong green pulse (515 nm, 30 μW, 50 μs) is used to scramble the local charge environment, before the check is repeated.

To investigate the effect of NV$^-$ ionisation on the nuclear spin data qubit, we require fast switching of the NV charge state along with efficient detection. In this section we design and implement a protocol which enables such studies.

The protocol is shown in Supplementary Fig. 7(a). We begin with a CR check, which we use to prepare the system in NV$^-$ (Check NV$^-$ (1)). At this point, we can utilise the previously described universal control to prepare the nuclear spin in a chosen state. Next, we apply a strong two-laser ionisation pulse. 50 nW of $\mathrm{E_y}$ and 500 nW of E' excitation are used, which are chosen to maintain predominantly NV$^-$ $m_s = 0$ projection while attempting ionisation. After this pulse, a second CR check is performed (Check NV$^-$ (2)). We proceed with the measurement only if this check returns 0 photon counts, which occurs with $\sim$ 10% (40%) probability after a 300 μs (1 ms) ionisation pulse. This outcome heralds the system in a dark state of the NV, which can be associated with either NV^0 or a significant detuning of the NV$^-$ transitions due to spectral diffusion.

We now perform the desired experiment on the nuclear spin, either allowing free evolution or applying RF driving. Next, we apply a strong yellow (575 nm) recharging pulse, using 500 nW for main text Figs. 3(a,b), and 1100 nW (the maximum attainable) for Fig. 3(c) to increase the recharging probability. After the recharging pulse, we apply spin-pump light to prepare the NV$^-$ $m_s = 0$ state and subsequently read-out the nuclear spin. Finally, we perform one more CR check (Check NV$^-$ (3)). The outcome of this check allows for post-selection of the nuclear spin read-out data upon finding the NV in the negative-charge state (retaining 82% of cases with the 575 nm pulse parameters used for Figs. 3(a,b): 1 ms, 500 nW, 85% for Fig. 3(c): 0.5 ms, 1100 nW). For post-selection, we discard data which lies close to the bright/dark discrimination threshold (see below). We only consider data for which the NV began in the negative charge-state ($>$ 13 counts in (1)), transferred to a dark state (0 counts in (2)), and then returned to the negative charge-state via the recharging pulse ($\geq$ 5 counts in (3)).

In Supplementary Fig. 7(b) we show example photon-count distributions from CR checks performed after preparing NV$^-$ (1), after heralding the dark state (2), and after applying a 1.1 μW, 0.5 ms recharging pulse (3). The mean number of photons detected in each case is 16.9, 0.3, and 13.7 respectively, clearly demonstrating the ability to switch between the bright and dark states. However, the slight reduction of mean counts for case (3) compared to case (1) indicates that the recharging process does not achieve unity success. We now study this process more carefully.

We first quantify the charge-state read-out fidelity. Considering the data shown in panels (1) and (2) of Supplementary Fig. 7(b), we maximise the quantity $F_{\mathrm{charge}} = \frac{1}{2}(F_{\mathrm{b|b}} + F_{\mathrm{d|d}})$, where $F_{i|j}$ is the probability to assign the 'bright' (b, NV$^-$) or 'dark' (d, NV^0 or off-resonant) state after attempting initialisation in that state. With a threshold of 3 counts (assign bright if ≥ 3 photons detected), we find $F_{\mathrm{charge}} = 98.81(4)\%$.

In Supplementary Fig. 7(c) we plot the NV$^-$ population after first preparing the dark state and then applying a 1 ms, 500 nW recharging pulse, for which we sweep the pulse frequency. The observation of two transitions corresponding to the spin-orbit branches of NV^0 confirms that this is the resonant recharging process [20, 21]. Here, the broader line observed for the higher-frequency resonance (lower spin-orbit branch of NV^0) is likely due to the polarisation of the yellow laser — which is fixed at an arbitrary value in these experiments — being biased towards linear horizontal [21]. Optimal recharging is achieved when working at the central frequency for this branch, here 521.247 THz. Note that the lifetime of the NV^0 orbital-state is short even at 4 K (sub-μs), and so it is sufficient to only address a single spin-orbit branch.

We now turn to the temporal dependence. In Supplementary Fig. 7(d) we show the NV$^-$ population as a function of the recharge pulse length, now at a (maximal) power of 1.1 μW. The population grows quickly, with a fitted time constant of 71(2) μs. However, beyond a maximum population of 88.6(6)% at $t = 0.55$ ms, the signal again decays. A possible explanation for this decay is spectral diffusion, caused by ionisation of nearby P1 centres by the yellow laser [22]. Note that significantly higher recharging probabilities were achieved in Ref. [21], where the diamond substrate contained significantly fewer impurities. In Supplementary Fig. 7(e), we focus on the first 500 μs of recharging, and probe the population in each of the NV^- spin states. We observe that the recharging laser induces fast spin-pumping into the $m_s = 0$ state, as expected due to the intersystem crossing. At $t = 500$ μs, the fraction of NV^- population in this state is 91.9(8)%. Note that this spin-pumping effect mitigates dephasing of the nuclear spin in the time between recharging and resonant spin-reset of the NV^- spin.

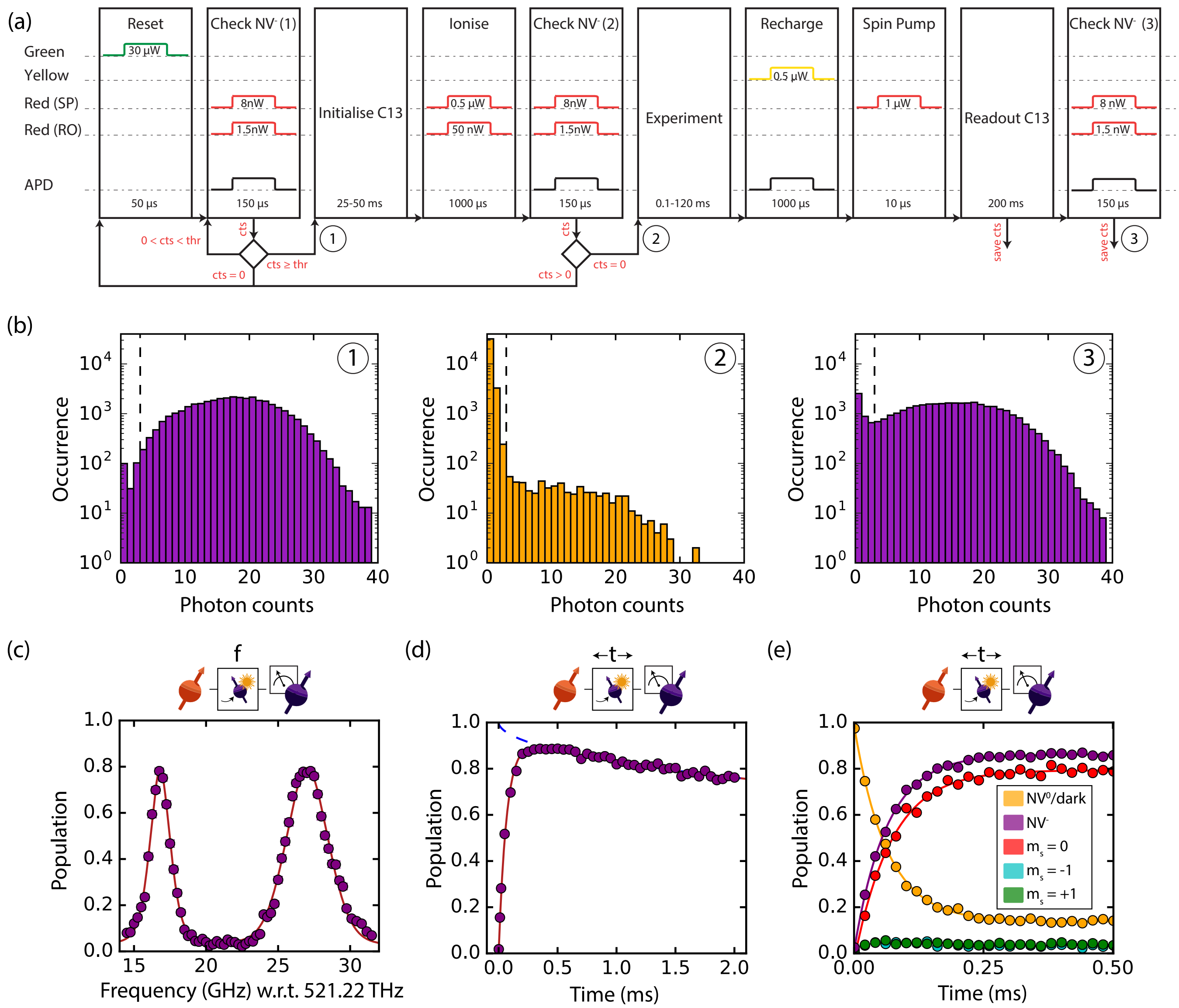

Supplementary Figure 7. **Charge-state switching:** (a) Flow diagram for the charge-state switching protocol, showing the decision logic used for bright- and dark-state heralding and optional post-selection. (b) Distribution of photon-counts from CR checks performed at the points (1), (2), (3) indicated in panel (a). (c) NV^- population as a function of the recharging pulse frequency, using a 1 ms pulse of 500 nW. Solid line is a fit to the sum of two Voigt profiles. (d) NV^- state population as a function of the recharging pulse duration, at 521.247 THz and 1.1 μW. Solid line is a fit to $F(t) = (1 - \exp[-t/\tau_1]) \cdot (\exp[-(t/\tau_2)^n]$, from which we find $\tau_1 = 71(2)$ μs, $\tau_2 = 22(4)$ ms and $n = 0.54(3)$. Dashed line shows the decay component, characterised by τ_2. (e) Populations in the NV^0/dark state, and in the differing spin-projections of the NV^- state as a function of the recharging pulse duration, again at 521.247 THz and 1.1 μW. Solid lines are fits to $F(t) = a + A\exp[-(t/\tau)^n]$. We find $\tau = \{73(7),63(1),63(1)\}$ μs, $n = \{1.0(1),1.00(1),1.00(1)\}$, for the $m_s = 0$, NV^0 and NV^- populations respectively.

Supplementary Note 9: Simulated performance of a weakly-coupled data qubit for distributed quantum information processing

In the main text, we present the simulated performance of two-qubit non-local operations and generation of four-qubit GHZ states between nuclear spin qubits hosted in disparate quantum network nodes. Here, we outline the models and methods used for these simulations. Further details can be found in the code implementation [23].

a. *Simulation parameters*

In Supplementary Tables 1-3, we list the relevant parameters, which are described in the following subsections. Supplementary Table 2 describes gate durations which are specific to a natural abundance ^{13}C device, alongside measured decoherence rates in such a device [12], whereas Supplementary Table 3 describes the numbers used and characterised in this work (0.01% ^{13}C).

b. *Node topology*

We assume that the NV centre has a star topology, where two qubit gates are only possible between the electron spin qubit and another qubit. Moreover, only the electron spin can act as the control for CNOT gates. Direct read-out is only possible for the electron spin qubit: other qubits must be read-out by first mapping their state to the electron spin. The protocols considered here require a maximum of three ^{13}C qubits per node.

c. *Decoherence*

Decoherence is modelled using two types of noise channels: the generalised amplitude damping channel and the phase damping channel [24], with characteristic timescales of T_1 and T_2 respectively. We assign different nuclear spin T_1 and T_2 values dependent on whether their associated electron spin is being used to generate inter-node entanglement at that point in the sequence.

The set of Kraus operators for the generalised amplitude damping channel is given by

$$\begin{aligned} K_{AD1} &= \sqrt{\frac{1}{2}} \begin{bmatrix} 1 & 0 \\ 0 & \sqrt{1-\gamma_1} \end{bmatrix}, \\ K_{AD2} &= \sqrt{\frac{1}{2}} \begin{bmatrix} 0 & \sqrt{\gamma_1} \\ 0 & 0 \end{bmatrix}, \\ K_{AD3} &= \sqrt{\frac{1}{2}} \begin{bmatrix} \sqrt{1-\gamma_1} & 0 \\ 0 & 1 \end{bmatrix}, \\ K_{AD4} &= \sqrt{\frac{1}{2}} \begin{bmatrix} 0 & 0 \\ \sqrt{\gamma_1} & 0 \end{bmatrix}, \end{aligned} \tag{3}$$

where $\gamma_1 = 1 - \exp(-t/T_1)$.

The set of Kraus operators for the phase damping channel is given by:

$$K_{PD1} = \begin{bmatrix} 1 & 0 \\ 0 & \sqrt{1-\gamma_2} \end{bmatrix}, \; K_{PD2} = \begin{bmatrix} 0 & 0 \\ 0 & \sqrt{\gamma_2} \end{bmatrix}, \tag{4}$$

where $\gamma_2 = 1 - \exp(-t/\bar{T}_2)$.

In Supplementary Tables 2 and 3, the T_1 times correspond to the experimentally measured decoherence times of the eigenstates of the Pauli-Z matrix ($|\uparrow\rangle$,$|\downarrow\rangle$), and correspond directly to the T_1 times used for the generalised amplitude damping channel of the model. The T_2 times correspond to the experimentally measured decoherence times of the eigenstates of the Pauli-X and Pauli-Y matrices ($|\mathrm{x}\rangle$,$|{-\mathrm{x}}\rangle$,$|\mathrm{y}\rangle$,$|{-\mathrm{y}}\rangle$). To account for the dephasing induced by the generalised amplitude damping channel, modified T_2 values must be used in the phase damping channel, which are given by:

$$\frac{1}{\bar{T}_2} = \frac{2}{T_2} - \frac{1}{T_1} \tag{5}$$

d. *Gates*

We model single-qubit gates as noiseless. We model noisy two-qubit gates using a depolarizing noise model:

$$N_{2Q}(\rho, p_g) = (1-p_g)\rho + \frac{p_g}{15} \sum_{\sigma_i,\sigma_j} (\sigma_i \otimes \sigma_j)\rho(\sigma_i \otimes \sigma_j)^\dagger, \tag{6}$$

where $\sigma_i, \sigma_j \in \{I, X, Y, Z\}$ and the sum is over all combinations of the Pauli operators σ_i, σ_j except for $\sigma_i = \sigma_j = I$.

For simplicity of compilation, we consider a gate-set consisting of the Pauli gates, the Hadamard gate, the CNOT gate and the CZ gate. SWAP gates are carried out using three CNOT gates. All single- and two-qubit gates have associated durations: after each operation, the appropriate T_1 and T_2 decoherence is applied to all idle qubits. Note that the universal gate-set offered by the NV centre platform can be compiled into this textbook gate-set at no additional cost in two-qubit gate count [25].

e. *NV-NV entanglement*

We model the creation of remote-entanglement (RE) links (i.e. NV-NV Bell pairs) following the single-click protocol [26]. The protocol produces states that we assume are of the form

$$\rho_{NV,NV} = (1-p_n) |\psi\rangle \langle\psi| + p_n |11\rangle \langle 11| . \tag{7}$$

with $|\psi\rangle = (|01\rangle + |10\rangle)/\sqrt{2}$ and p_n a parameter that we call the network error, arising from events in which both NVs emitted a photon. That is, we assume the intrinsic infidelity associated with the single-photon scheme dominates over other error sources such as imperfect visibility [1]. The single-click protocol succeeds with probability p_{RE}.

In simulation, each time a RE link must be generated, Monte-Carlo methods are used to determine the number of entangling attempts n_{RE} before success. The decoherence channels are then applied to all idle qubits with an associated duration of $t_{\mathrm{ent}} = n_{\mathrm{RE}} T_{RE}$, where T_{RE} is the duration of each entangling primitive.

The results presented in Fig. 4(c) of the main text are averaged over 500,000 repetitions, whereas those in Fig. 4(d) use 100,000 repetitions, aside from the Expedient protocol for $N_{1/\mathrm{e}} = 2{\cdot}10^3$, for which only 10,000 repetitions are used due to the low protocol success rate.

f. Measurement noise

We restrict measurements to the Z-basis. To measure the qubits in the X-basis, we apply a Hadamard gate before the measurement. The gate duration time of this additional operation is included in the simulations.

We model (single qubit) measurement errors by projecting onto the opposite eigenstate of the measured operator. Measurement errors are characterised by the probability p_m of an incorrect projection.

g. Dynamical decoupling

To mitigate dephasing of both communication and data qubits due to quasi-static noise sources (for example, due to spin-bath interactions or magnetic field fluctuations), a dynamical decoupling scheme is accounted for in the sequencing of all operations. We model this process by only applying operations at intervals of a basic echo sequence on the data qubits: $\tau - \pi - \tau$. Here, π denotes a π-pulse being applied to the system, and τ is the inter-pulse delay time. Operations are only allowed in between the echo sequences of each node; consecutive operations in the same node are allowed, after which the decoupling sequence is restarted. We set τ equal to the duration of 2500 entangling attempts for the purified sample and a τ equal to the duration of 250 entangling attempts for the natural abundance sample. The π-pulse duration is set to $13 \cdot 10^{-3}$ seconds for the purified sample and $1 \cdot 10^{-3}$ seconds for the natural abundance sample. Due to the faster gate operations associated with the communication qubits, we assume that refocusing points of their own decoupling sequences can be simply matched to those of the data qubits.

h. Non-local CNOT operations

In Fig. 4(c) of the main text, we present the average fidelity of a non-local CNOT operation. Here, we use the parameters given in Supplementary Tables 1 and 3, but sweep the values of $T1^n_{RE} = T2^n_{RE} = N_{1/\mathrm{e}} \cdot T_{RE}$. The average fidelity of the operation is calculated by determining the entanglement fidelity following the relation given in Ref. [27]. We do not show the results when using the faster gate and measurement durations (Supplementary Table 2), because a negligible difference is observed. For example, for $N_{1/\mathrm{e}} = 83{,}333$, we find an average fidelity of 0.7899, compared with 0.7890 when using the slower durations.

i. GHZ-creation protocols

In this section, we discuss the three GHZ creation protocols used in Fig. 4(d) of the main text. The circuit diagrams of the protocols are depicted in Supplementary Fig. 8. In each node, the first (purple) qubit indicates the electron qubit of the NV centre (i.e., the communication qubit), with the other qubits indicating ^{13}C spins (‘memory’ and ‘data’ qubits). The memory qubits are used to store intermediate states required to create the GHZ state. When the GHZ state is created, it can be consumed to non-locally perform a weight-4 Pauli measurement on qubits of a distributed error-correcting code, e.g., the surface code [28, 29]. In the diagrams of Supplementary Fig. 8, the inner-most ^{13}C is the data qubit of the code (i.e., it would be a constituent of an encoded logical qubit).

The Plain protocol is the most simple protocol to create a 4-qubit GHZ state out of Bell pairs: it only requires three pairs. The local operations of this protocol ‘fuse’ the three pairs into the GHZ state. Fusion takes place with Block B.2 from the legend: this operation fuses two entangled states that do not overlap in any of the nodes with the aid of a Bell pair that is consumed in the process. Feed-forward operations based on this Bell-state measurement lead to protocol success with unit probability.

As mentioned above, RE links can only be created between the electron qubits. Hence, the states of the electron qubits must be swapped with those of data qubits (‘stored’) at some point in all of the protocols. In the Plain protocol, this occurs after the first pair of RE links are created: the electron qubits of nodes A, C are stored such that it is possible to generate a third RE link between nodes A and C.

The Modicum protocol uses one additional Bell pair compared to Plain. This additional pair is used to distill the 4-qubit GHZ state. This distillation step is probabilistic; if successful it increases the state fidelity. However, if it fails, the GHZ state is discarded and the protocol restarts from scratch. Fusion of the Bell pairs takes place in Modicum with Block B.1 (both in nodes A and C in Supplementary Fig. 8), which describes fusion of two entangled states that overlap in one network node. Distillation takes place with Block A.2 in nodes B and D, which essentially measures a stabilizer of the desired pure entangled state. In particular, Block A.2 is known in the literature as 'single selection' [30]. The operation is successful if the measurement results coincide: this corresponds to the +1 outcome of the stabilizer measurement. In case of an odd measurement combination, the distillation operation fails, and the protocol returns to the indicated 'failure reset level' (indicated with 'frl' in the legend). The Modicum protocol is identified with the dynamic programming algorithm presented in [31], and is similar to the protocol that creates one of the two GHZ states of the 'Basic' protocol in [29].

The Expedient protocol [28] uses 22 Bell pairs to create the GHZ state. Compared to the Plain protocol, the additional 19 Bell pairs are used for distillation purposes. This can be either for distillation of Bell pairs before they are fused to form the GHZ state, or for distillation of the GHZ state after it is created. Distillation takes place with Block A.2, but also with Block C.1 and Block C.2. Block C.1 can be understood as an operation that performs two distillation steps by consuming two ancillary Bell pairs. This block is known in the literature as the 'double selection' distillation protocol [30]. Block C.2 essentially performs three distillation steps by consuming three Bell pairs. Depending on where in the circuit the distillation steps occur, failure of a step means the entire protocol has to start from scratch, or only a specific branch of the protocol has to be carried out again. Finally, similar to the Plain protocol, this protocol uses Block B.2 to fuse three Bell pairs into a GHZ state. This takes place between distillation blocks A.2 and C.2.

Parameter	Description	Values
General parameters		
$\mathbf{p_g}$	Gate error probability	0.01
$\mathbf{p_m}$	Measurement error probability	0.01
$\mathbf{p_n}$	Network error probability	0.1
$\mathbf{p_{RE}}$	RE success probability	0.0001
$\mathbf{T_{meas}}$	Measurement duration	$4.0 \cdot 10^{-6}$ s
$\mathbf{T_{RE}}$	RE duration	$6.0 \cdot 10^{-6}$ s
$\mathbf{T^{e}_{X}}$	Electron X gate duration	$0.14 \cdot 10^{-6}$ s
$\mathbf{T^{e}_{Y}}$	Electron Y gate duration	$0.14 \cdot 10^{-6}$ s
$\mathbf{T^{e}_{Z}}$	Electron Z gate duration	$0.10 \cdot 10^{-6}$ s
$\mathbf{T^{e}_{H}}$	Electron H gate duration	$0.10 \cdot 10^{-6}$ s

Supplementary Table 1. General system parameters as used for the simulations presented in Figs. 4(c,d) of the main text.

^{13}C decoherence parameters (Ref. [12])		
$\mathbf{T1^{n}_{idle}}$	^{13}C T_1 when idle	300 s
$\mathbf{T1^{n}_{RE}}$	^{13}C T_1 during RE attempts	0.03 s
$\mathbf{T2^{n}_{idle}}$	^{13}C T_2 when idle	10 s
$\mathbf{T2^{n}_{RE}}$	^{13}C T_2 during RE attempts	0.012 s
$\mathbf{T2^{e}_{idle}}$	Electron T_2 when idle	1.0 s
1.1% ^{13}C gate durations		
$\mathbf{T^{C}_{X}}$	^{13}C X gate duration	$1.0 \cdot 10^{-3}$ s
$\mathbf{T^{C}_{Y}}$	^{13}C Y gate duration	$1.0 \cdot 10^{-3}$ s
$\mathbf{T^{C}_{Z}}$	^{13}C Z gate duration	$0.5 \cdot 10^{-3}$ s
$\mathbf{T^{C}_{H}}$	^{13}C H gate duration	$0.5 \cdot 10^{-3}$ s
$\mathbf{T_{CNOT}}$	CNOT gate duration	$0.5 \cdot 10^{-3}$ s
$\mathbf{T_{CZ}}$	CZ gate duration	$0.5 \cdot 10^{-3}$ s
$\mathbf{T_{SWAP}}$	SWAP gate duration	$1.5 \cdot 10^{-3}$ s

Supplementary Table 2. Decoherence timescales as measured in Ref. [12], and typical gate durations for such a device (1.1% ^{13}C) [6], as used for the simulations presented in Fig. 4(d) of the main text (labelled by $N_{1/e} = 2{\cdot}10^3$, the $T2^n_{\rm RE}$ decay).

^{13}C decoherence parameters (this work)		
$\mathbf{T1^{n}_{idle}}$	^{13}C T_1 when idle	300 s
$\mathbf{T1^{n}_{RE}}$	^{13}C T_1 during RE attempts	1.2 s
$\mathbf{T2^{n}_{idle}}$	^{13}C T_2 when idle	10 s
$\mathbf{T2^{n}_{RE}}$	^{13}C T_2 during RE attempts	1.2 s
$\mathbf{T2^{e}_{idle}}$	Electron T_2 when idle	1.0 s
0.01% ^{13}C gate durations		
$\mathbf{T^{C}_{X}}$	^{13}C X gate duration	$13 \cdot 10^{-3}$ s
$\mathbf{T^{C}_{Y}}$	^{13}C Y gate duration	$13 \cdot 10^{-3}$ s
$\mathbf{T^{C}_{Z}}$	^{13}C Z gate duration	$6.5 \cdot 10^{-3}$ s
$\mathbf{T^{C}_{H}}$	^{13}C H gate duration	$6.5 \cdot 10^{-3}$ s
$\mathbf{T_{CNOT}}$	CNOT gate duration	$25 \cdot 10^{-3}$ s
$\mathbf{T_{CZ}}$	CZ gate duration	$25 \cdot 10^{-3}$ s
$\mathbf{T_{SWAP}}$	SWAP gate duration	$75 \cdot 10^{-3}$ s

Supplementary Table 3. Decoherence timescales as measured in this work, and associated gate durations (0.01% ^{13}C device), as used for the simulations presented in Figs. 4(c) (see *"Non-local CNOT operations"*) and 4(d) (labelled by $N_{1/e} = 2{\cdot}10^5$, the $T2^n_{\rm RE}$ decay) of the main text.

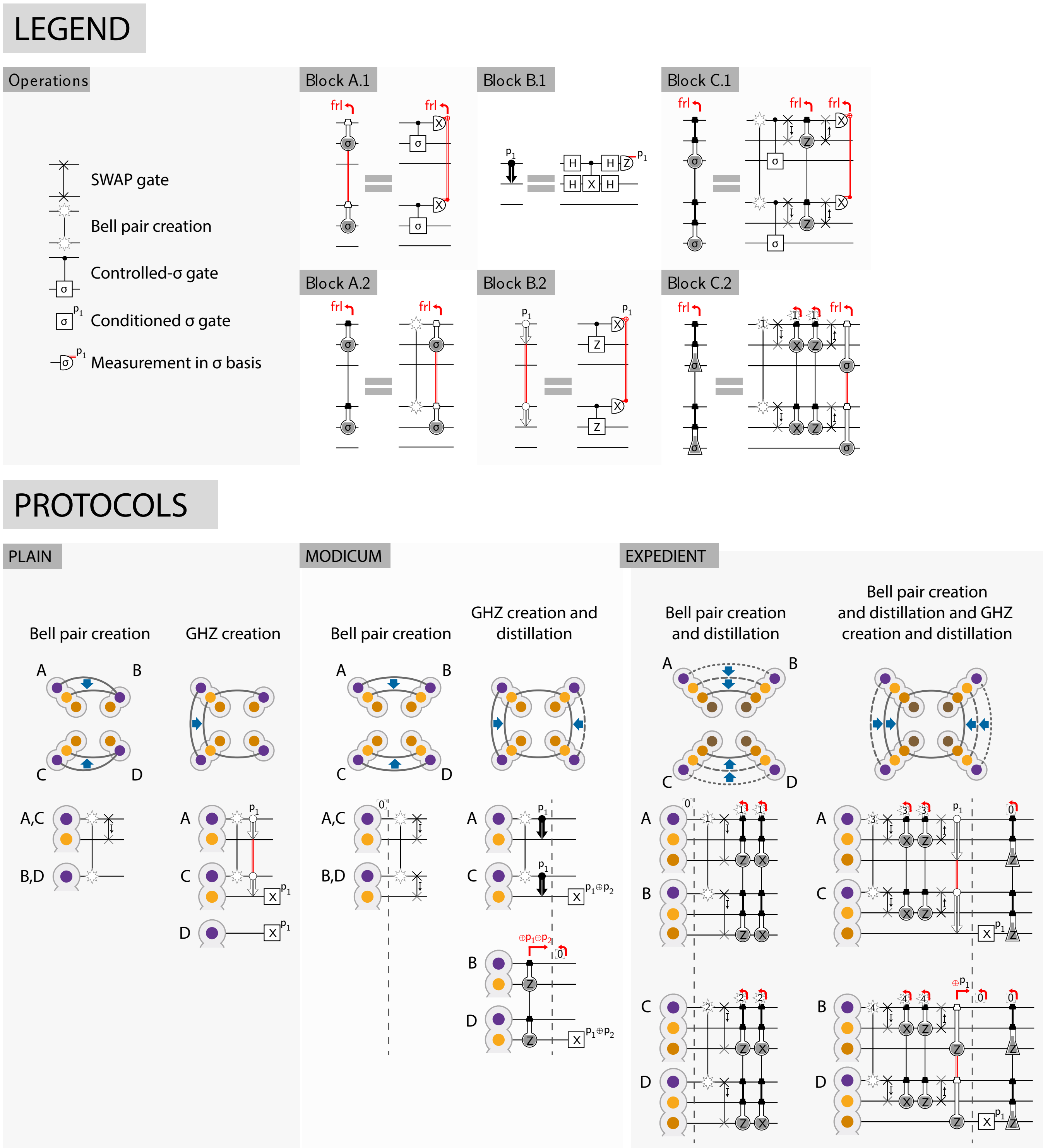

Supplementary Figure 8. Circuit diagrams of the three GHZ creation protocols used in the simulations. Bell states are generated in the form of Eq. 7, followed by an X-gate on their second qubit to turn them into noisy versions of the $(|00\rangle + |11\rangle)/\sqrt{2}$ state. 'Plain' uses three Bell pairs to create a 4-qubit GHZ state. 'Modicum' uses a fourth Bell pair to increase the GHZ fidelity with a distillation step. 'Expedient' [28] uses 22 Bell pairs and has many (intermediate) distillation steps. Details of those steps are given in the text. The schematics above the circuits show four network nodes (A,B,C,D) comprising an electron spin (purple) and up to three nuclear spins (orange tones).

[1] P. C. Humphreys *et al.* Deterministic delivery of remote entanglement on a quantum network. *Nature* **558**, 268–273 (2018)
[2] D. Hucul *et al.* Modular entanglement of atomic qubits using photons and phonons. *Nat. Phys.* **11**, 37–42 (2015)
[3] T. H. Taminiau *et al.* Detection and Control of Individual Nuclear Spins Using a Weakly Coupled Electron Spin. *Phys. Rev. Lett.* **109**, 137602 (2012)
[4] J. M. Boss *et al.* One-and two-dimensional nuclear magnetic resonance spectroscopy with a diamond quantum sensor. *Phys. Rev. Lett.* **116**, 197601 (2016)
[5] T. H. Taminiau, J. Cramer, T. van der Sar, V. V. Dobrovitski, and R. Hanson. Universal control and error correction in multi-qubit spin registers in diamond. *Nat. Nanotechnol.* **9**, 171–176 (2014)
[6] C. E. Bradley *et al.* A Ten-Qubit Solid-State Spin Register with Quantum Memory up to One Minute. *Phys. Rev. X* **9**, 031045 (2019)
[7] J. Cramer *et al.* Repeated quantum error correction on a continuously encoded qubit by real-time feedback. *Nat. Commun.* **7**, 1–7 (2016)
[8] P. C. Maurer *et al.* Room-Temperature Quantum Bit Memory Exceeding One Second. *Science* **336**, 1283–1286 (2012)
[9] A. Dréau, P. Spinicelli, J. Maze, J.-F. Roch, and V. Jacques. Single-shot readout of multiple nuclear spin qubits in diamond under ambient conditions. *Phys. Rev. Lett.* **110**, 060502 (2013)
[10] G.-Q. Liu *et al.* Single-shot readout of a nuclear spin weakly coupled to a nitrogen-vacancy center at room temperature. *Phys. Rev. Lett.* **118**, 150504 (2017)
[11] N. Kalb, P. C. Humphreys, J. J. Slim, and R. Hanson. Dephasing mechanisms of diamond-based nuclear-spin memories for quantum networks. *Phys. Rev. A* **97**, 062330 (2018)
[12] M. Pompili *et al.* Realization of a multinode quantum network of remote solid-state qubits. *Science* **372**, 259–264 (2021)
[13] L. Robledo, H. Bernien, I. van Weperen, and R. Hanson. Control and Coherence of the Optical Transition of Single Nitrogen Vacancy Centers in Diamond. *Phys. Rev. Lett.* **105**, 177403 (2010)
[14] P. Siyushev, H. Pinto, A. Gali, F. Jelezko, and J. Wrachtrup. Optically Controlled Switching of the Charge State of a Single Nitrogen-Vacancy Center in Diamond at Cryogenic Temperatures. *Phys. Rev. Lett.* **110**, 167402 (2013)
[15] H. Bernien *et al.* Heralded entanglement between solid-state qubits separated by three metres. *Nature* **497**, 86–90 (2013)
[16] N. Kalb *et al.* Experimental creation of quantum Zeno subspaces by repeated multi-spin projections in diamond. *Nat. Commun.* **7**, 13111 (2016)
[17] W. Pfaff *et al.* Unconditional quantum teleportation between distant solid-state quantum bits. *Science* **345**, 532–535 (2014)
[18] J. Johansson, P. Nation, and F. Nori. QuTiP: An open-source Python framework for the dynamics of open quantum systems. *Comput. Phys. Commun.* **183**, 1760–1772 (2012)
[19] A. Reiserer *et al.* Robust Quantum-Network Memory Using Decoherence-Protected Subspaces of Nuclear Spins. *Phys. Rev. X* **6**, 021040 (2016)
[20] M. S. Barson, E. Krausz, N. B. Manson, and M. W. Doherty. The fine structure of the neutral nitrogen-vacancy center in diamond. *Nanophotonics* **8**, 1985 - 1991 (2019)
[21] S. Baier *et al.* Orbital and Spin Dynamics of Single Neutrally-Charged Nitrogen-Vacancy Centers in Diamond. *Phys. Rev. Lett.* **125**, 193601 (2020)
[22] F. Heremans, G. Fuchs, C. Wang, R. Hanson, and D. Awschalom. Generation and transport of photoexcited electrons in single-crystal diamond. *Appl. Phys. Lett.* **94**, 152102 (2009)
[23] The code implementation for the noisy quantum network simulations can be found at https://doi.org/10.4121/16887658.v3.
[24] M. Nielsen, and I. Chuang. Quantum computation and quantum information. *Cambridge University Press* (2000)
[25] M. H. Abobeih *et al.* Fault-tolerant operation of a logical qubit in a diamond quantum processor. *Nature* **606**, 884–889 (2022)
[26] C. Cabrillo, J. I. Cirac, P. García-Fernández, and P. Zoller. Creation of entangled states of distant atoms by interference. *Phys. Rev. A* **59**, 1025–1033 (1999)
[27] M. A. Nielsen. A simple formula for the average gate fidelity of a quantum dynamical operation. *Phys. Lett. A* **303**, 249–252 (2002)
[28] N. H. Nickerson, Y. Li, and S. C. Benjamin. Topological quantum computing with a very noisy network and local error rates approaching one percent. *Nat. Commun.* **4**, 1–5 (2013)
[29] N. H. Nickerson, J. F. Fitzsimons, and S. C. Benjamin. Freely scalable quantum technologies using cells of 5-to-50 qubits with very lossy and noisy photonic links. *Phys. Rev. X* **4**, 041041 (2014)
[30] K. Fujii, and K. Yamamoto. Entanglement purification with double selection. *Phys. Rev. A* **80**, 042308 (2009)
[31] S. de Bone, R. Ouyang, K. Goodenough, and D. Elkouss. Protocols for creating and distilling multipartite GHZ states with Bell pairs. *IEEE Trans. On Quantum Eng.* **1**, 1-10 (2020)